Isoscalar electric multipole strength in ^{12}C

Bency John,* Y. Tokimoto, Y.-W. Lui, H. L. Clark, X. Chen, and D. H. Youngblood

Cyclotron Institute, Texas A&M University, College Station, Texas 77843, USA

The excitation region in ^{12}C below $E_x = 45$ MeV was studied using 240 MeV α-particle scattering. Elastic scattering was measured from $\theta_{c.m.} = 3.8°$ to $49.4°$ and density dependant folding optical model parameters were obtained. Inelastic scattering to the 4.44 MeV 2^+, 7.65 MeV 0^+, 9.64 MeV 3^-, 10.3 MeV 0^+, and 10.84 MeV 1^- states was measured and $B(EL)$ values obtained. Inelastic scattering exciting ^{12}C to 10 MeV $\leqslant E_x \leqslant 12.5$ MeV was measured from $1.4° \leqslant \theta_{c.m.} \leqslant 10°$ and to 12.5 MeV $\leqslant E_x \leqslant 45$ MeV from $1.4° \leqslant \theta_{c.m.} \leqslant 16°$ and $E0$, $E1$, $E2$, and $E3$ strength distributions were obtained. Strength was identified corresponding to 27 ± 5, 78 ± 9, and $51 \pm 7\%$ of the isoscalar $E0$, $E1$, and $E2$ energy weighted sum rule (EWSR), respectively, with centroids of 21.9 ± 0.3, 27.5 ± 0.4, and 22.6 ± 0.5 MeV and rms widths of 4.8 ± 0.5, 7.6 ± 0.6, and 6.8 ± 0.6 MeV. Less than 7% of the $E3$ EWSR strength was identified.

DOI: 10.1103/PhysRevC.68.014305   PACS number(s): 25.55.Ci, 24.30.Cz, 27.20.+n, 21.10.Re

I. INTRODUCTION

Isoscalar excitation of the ^{12}C nucleus is an important source of information on its structure. In the collective liquid drop model, isoscalar excitations of different multipolarities have been interpreted as arising due to in-phase oscillations ($T=0$) of the proton and neutron fluids. The isoscalar monopole resonance (ISGMR or $E0$; $L=0$, $T=0$, $\sigma=0$) is a density oscillation and its energy is directly related to the compressibility of nuclear matter [1]. The isoscalar dipole resonance (ISGDR or $E1$; $L=1$, $T=0$, $\sigma=0$) is also a density oscillation traveling back and forth through the nucleus along a definite direction [2]. Higher multipolarities are shape oscillations.

The structure of ^{12}C has been the subject of two recent shell model calculations. In the first of these [3], an effective interaction gave good results for the ground state and the 4.44 MeV 2^+ first excited state but several of the higher states were not reproduced well. In the second study the properties of ^{12}C were obtained with a no-core nuclear shell model calculation with a realistic nucleon-nucleon interaction [4]. Some of the properties of the first excited state and of some higher states were reproduced moderately well. In this calculation, the GQR in ^{12}C was predicted to be in the 37 to 47 MeV range. Many higher $T=0$ states in ^{12}C show evidence [5,6] for α cluster components which would not be reproduced by such shell model calculations. Such components have been interpreted using the bosonic nature of the alpha clusters. The 7.65 MeV 0^+ second excited state of ^{12}C has been described recently as a Bose-Einstein condensation state of α clusters [7]. Isoscalar states higher in energy and of different multipolarities, whether or not they yield to such interpretations, can be expected to give insight into the nucleon localization behavior because they arise due to *in-phase* spin saturated motion ($T=0,\sigma=0$) of the nucleons.

Properties of isoscalar states have been extracted from experiments traditionally by using the collective model. The properties of collective modes in a diffused nuclear medium is an evolving topic [8] and efforts are planned with radioactive ion beams to measure them. In such studies, the first results will be with lighter nuclei and accurate data on ^{12}C collective modes can serve as a guide. By itself, ISGMR and ISGDR data in ^{12}C might provide important inputs to the surface corrections applied to compressibility of a finite nucleus K_A to arrive at nuclear matter compressibility coefficient K_{nm}.

Although the structure of ^{12}C has been studied experimentally with a number of probes, there have been few studies of high-lying isoscalar $E0$ and $E2$ strength and no reports of small-angle scattering experiments looking for high-lying isoscalar $E1$ strength. No concentration of high lying isoscalar $E0$ and $E2$ strengths comparable to that of heavier nuclei has been seen in ^{12}C.

Riedesel *et al.* [9] located less than 15% of the $E2$ energy weighted sum rule (EWSR) in the range $20 \leqslant E_x \leqslant 30$ MeV with 104 MeV α-particle inelastic scattering. Lebrun *et al.* [10] reported 4.3% of the $E0$ EWSR in a broad peak at 20.3 MeV using inelastic ^{3}He scattering and Eyrich *et al.* [11] reported $5 \pm 2\%$ of the $E0$ EWSR between $E_x = 19$ and 21.5 MeV using inelastic ^{6}Li scattering. Youngblood *et al.* [12] located $14.5 \pm 4.0\%$ of the isoscalar $E0$ EWSR strength in ^{12}C between $E_x = 14$ MeV and $E_x = 30$ MeV using 240 MeV α-particle inelastic scattering.

Youngblood *et al.* [12] used a spectrum subtraction technique to highlight the $E0$ strength, however, this technique is sensitive to experimental background and the presence of other multipolarities. Also the analysis was performed using deformed potential calculations with ^{28}Si parameters which may distort the strength distribution. In recent studies of high lying isoscalar $E0$, $E1$, and $E2$ strengths in ^{28}Si [13], ^{40}Ca [14], and ^{24}Mg [15], a multipole component analysis of the excitation energy spectra measured at forward angles replaced the spectrum subtraction technique. In place of the deformed potential DWBA calculations, more accurate folding potential DWBA calculations were used. These improvements resulted in the identification of most of the $E0$ and $E2$

————
*Present address: Nuclear Physics Division, Bhabha Atomic Research Center, Mumbai-400085, India.

TABLE I. Experimental setup. (GR: giant resonance, EL: elastic.)

Run	Type	θ_{sp} (deg.)	Slit $\theta \times \phi$	Detector length (cm)	ϕ measurement	E_x range (MeV)	C foil thickness (mg/cm^2)
1	GR	0	4°×4°	30	No	$3 < E_x < 35$	2.0
2	EL	3.5,5.5	4°×2°	60	No	$-10 < E_x < 45$	2.0
	GR	0,3.5	4°×4°	60	No	$7 < E_x < 62$	2.0
3	GR	0,4	4°×4°	60	No	$7 < E_x < 62$	2.0
4	EL	4,6,8,10, 12,14,16, 18,20,22, 24,26,29	4°×2°	60	No	$-10 < E_x < 45$	4.02
	EL	32,35	4°×4°	60	No	$-10 < E_x < 45$	4.02
5	EL	4,6,8	4°×4°	60	No	$-10 < E_x < 45$	8.6
	GR	0	5°×5°	60	Yes	$9 < E_x < 55$	8.6
	GR	4,6,8,10	4°×4°	60	Yes	$9 < E_x < 55$	8.6

strength and allowed extraction of multipole distributions with better resolution than previously achieved, and resulted in strengths for low lying states in agreement with electromagnetic measurements. Extension of this method to ^{12}C should provide more accurate estimates of the isoscalar $E0$ and $E2$ strengths and new information on the isoscalar $E1$ strength.

States lying above the three-α-decay threshold energy (7.27 MeV) and below the "giant resonance" energy have been studied in the past primarily to reveal their α and electromagnetic decay characteristics and branching ratios. The 0_3^+ state, a broad resonance at 10.3 ± 0.3 MeV with a width around 3 MeV, and other levels above 10 MeV make this a region of overlapping levels. Interesting results may emerge if inelastic α scattering data for this excitation range could also be analyzed using the multipole components method. Particularly, the exact location of the 0_3^+ and 2_2^+ states would provide important inputs to calculations of nuclear astrophysical [16] and nuclear clustering [5,6] interests.

We report here new data of 240 MeV α-particle elastic and inelastic scattering on ^{12}C up to an excitation energy of $E_x = 45$ MeV. Above $E_x = 45$ MeV the "pickup-breakup" peaks from the (α, ^{5}Li) and (α, ^{5}He) reactions with subsequent decay of mass five products into an α particle and a nucleon hamper the determination of multipole strengths. Results of the multipole analysis performed with isoscalar 0^+, 1^-, 2^+, 3^-, and 4^+ components are presented. This excitation energy range is sufficiently broad to observe important features of the isoscalar $E0$, $E1$, and $E2$ strength distributions although the complete sum rule strengths have not been observed. Many isoscalar $E3$ and $E4$ states have also been identified. The results are discussed in light of the collective model and other relevant experimental results reported in the literature.

II. EXPERIMENTAL TECHNIQUE

Experiments were carried out using beams of 240 MeV α particles from the Texas A&M K500 superconducting cyclo-

tron and the multipole-dipole-multipole (MDM) spectrometer. Beam was delivered to the spectrometer through a beam analysis system having two bends of 88° and 87° [17]. The beam was limited by the slits after the first bend, and the second bend was used for clean up, with slits located so as not to intercept the primary beam. Table I lists different setups used in experiments carried out on five separate occasions to obtain data on elastic, inelastic, and giant resonance scattering. For giant resonance (GR) runs, the dipole field of the spectrometer was set such that the elastically scattered events did not reach the active region of the detector. In elastic scattering runs, the dipole field was set to allow elastic and low lying inelastic events to reach the detector's active region. The central angle of the spectrometer (θ_{sp}) was varied from 0° to 10° for GR measurements and from 3.5° to 35° for elastic scattering measurements. The solid angle defining slit at the entrance of the spectrometer had horizontal and vertical acceptances of 4° (4°×4° slit) for GR runs except for one run where a 5°×5° slit was used at $\theta_{sp} = 0°$. In elastic scattering runs either a 4°×2° slit or a 4°×4° slit was used at the more forward angles, and a 4°×4° slit was used at larger angles. The scattering angle was determined by ray tracing. The spectrometer angle θ_{sp} was varied in steps of 2°, except above $\theta_{sp} = 26°$ where 3° steps were used. The first nonzero angle was $\theta_{sp} = 3.5°$.

In run 1, a 30 cm long focal plane detector described in Ref. [18] was used which measured horizontal position and angle and provided particle identification. In runs 2–4, a similar detector 60 cm long [12,19] was used. In run 5, drift chambers were added before and after the 60 cm long horizontal detector to measure vertical position and the out of plane angle ϕ. When θ_{sp} was set to 0°, the primary beam was stopped in front of the 30 cm detector during run 1, while during runs 2–5 the beam passed beside the 60 cm detector and was stopped on a carbon block inside a shielded Faraday cup behind the detector. When $3.5° < \theta_{sp} < 6°$, the beam was stopped on an insulated Ta block beside the solid angle defining slit; at larger angles the beam was stopped on a Faraday cup in the target chamber. The horizontal position and
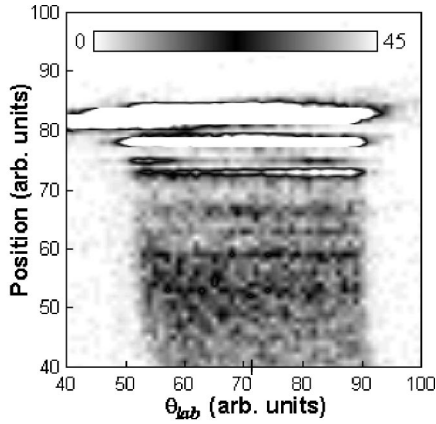
FIG. 1. A two dimensional plot of position versus θ_{lab} for ^{12}C(α,α') taken at $E_\alpha = 240$ MeV. The dipole field of the spectrometer was set for an elastic run with θ_{sp} set at 4° (run 5). On the θ_{lab} axis the location of 4° is indicated by a vertical marker at about 72 units and the forward angles are on the left side of this marker. The relative yield is shown by a folded-linear-scale of intensity indicated in the inset. Elastically scattered events appear as a broad band above 80 units in position.

FIG. 2. Same as in Fig. 1 except that dipole field was set for a GR run and θ_{sp} was 0° (run 2). On the θ_{lab} axis the location of 0° is indicated by a vertical marker at about 63 units.

angle resolutions were around 0.9 mm and 0.09°, respectively, but were somewhat worse in run 1 at 0° because of a high background rate due to neutrons and gamma rays from the Faraday cup located immediately in front of the detector. The range of excitation energy measured depended on the detector geometries and the dipole field and is summarized in Table I.

Self-supporting natural carbon foils of thicknesses 2, 4.02, and 8.6 mg/cm^2 were used as targets. The first two targets were made of layers of vacuum evaporated carbon foils and the third target was a graphite foil. The graphite foil was baked before use to minimize volatile impurities. Data were also taken with ^{24}Mg and ^{28}Si targets at the actual field settings used in the experiments for energy calibrations. Details of the momentum and angle calibrations are given in Ref. [19].

III. DATA ANALYSIS AND RESULTS

Two-dimensional spectra of position versus θ_{lab} obtained during elastic ($\theta_{sp} = 4°$) and GR runs ($\theta_{sp} = 0°$) are shown in Figs. 1 and 2. In Fig. 2, the 4.44 MeV 2^+ state can be seen only over a very narrow angle range, and the 7.65 MeV 0^+ state is seen over θ_{lab} from about 40 to 90 units. The tail coming down vertically from about 90 units is due to α particles scattering off the wall of the chamber inside the dipole, accidentally coinciding at about $\theta_{lab} = 90$ units with the 7.65 MeV band. This "tail" is outside the possible angle range for α particles that came through the entrance slit and did not subsequently scatter inside the spectrometer and hence these events are excluded when scattering angle cuts are made to obtain the energy spectra. The gray conical portion at the bottom is due to events in the range where the effective acceptance of the spectrometer varies rapidly with angle.
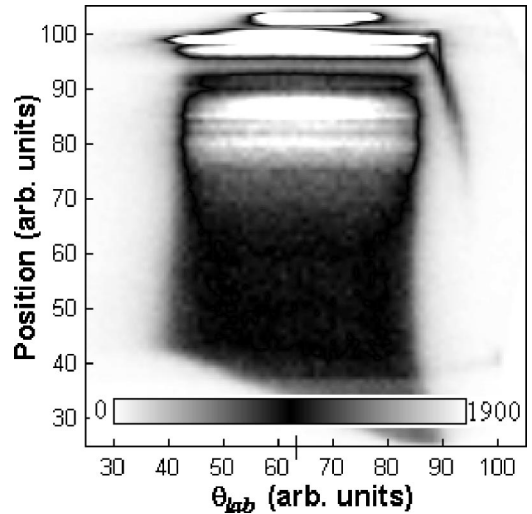
Cross sections were obtained from the charge collected, target thickness, dead time and known solid angle. The cumulative uncertainties in target thickness, solid angle, etc., result in about a ±10% uncertainty in absolute cross sections. Each data set was divided into ten angle bins, each corresponding to $\Delta\theta_{lab} \sim 0.4°$ using the angle obtained from ray tracing. The average angle for each bin was obtained by integrating over the height of the solid angle defining slit and the width of the angle bin.

Energy spectra showing elastic and inelastic scattering below $E_x = 24$ MeV at $\theta_{c.m.} = 3.8°$ and 5.3° are shown in Fig. 3. The first four prominent peaks can be identified as the ground, 4.44, 7.65, and 9.64 MeV states. There are very few counts in the region where scattering off any hydrogen impurity would be expected [$E_x = 2.35$ MeV in Fig. 3(a)] indicating that this target is nearly free of water vapor contaminant. A weak peak at $E_x \sim 3.7$ MeV is presumably due to the excitation of an unresolved group of states in ^{13}C. Spectra obtained in two runs with $\theta_{sp} = 0°$ (runs 2 and 5, respectively) for $\theta_{c.m.} = 1.4°$ are shown in Figs. 4(a) and 4(b). A ϕ gate was used in analysis of the data from run 5 to limit vertical acceptance to 4°. Data taken in run 2 with a vertical acceptance of 4° were analyzed without ϕ information. The excellent agreement between the spectra in the two runs shows the absence of significant slit scattering in the data taken in run 2.

Cross sections for elastic scattering and for inelastic scattering exciting the 4.44 MeV state were obtained by summing the counts in the appropriate peaks. The cross sections of states in the region $7.6 \leq E_x \leq 13$ MeV were determined by a least squares fit including known peaks in this region. An empirical peak shape determined from the shape of the peak for the 4.44 MeV state was used for the narrow states and a Gaussian shape was used for the broad 10 MeV 0^+ state. Background was assumed to be zero. Fits obtained for two angles are shown in Fig. 5. In addition to known ^{12}C states in this excitation range [20], a weak peak at 6.86 MeV due to a ^{13}C state and in some spectra two ^{16}O states at $\sim$6.0 MeV
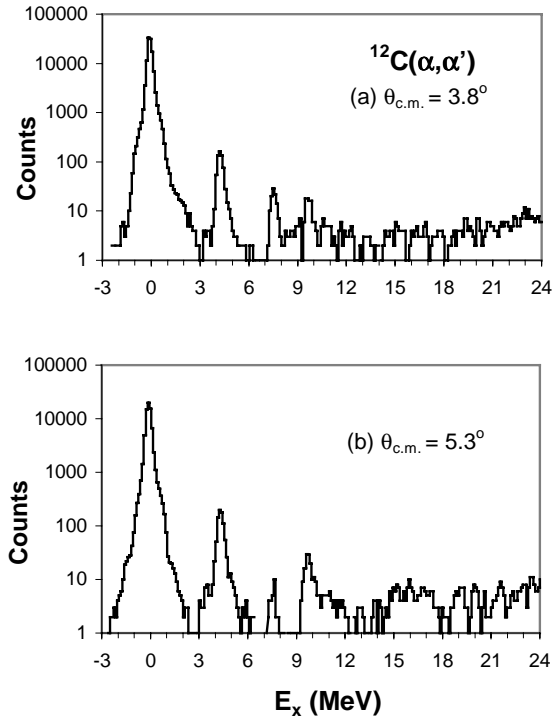
FIG. 3. α spectra obtained for $^{12}C(\alpha, \alpha')$ at $E_\alpha = 240$ MeV at average center of mass angles (a) $\theta_{c.m.} = 3.8°$ and (b) $\theta_{c.m.} = 5.3°$ during an elastic scattering run.

were also present. The parameters obtained for the peak due to the 0_3^+ state are $E_x = 9.8^{+0.4}_{-0.2}$ MeV and $\Gamma = 2.7 \pm 0.3$ MeV, respectively which are in agreement with those measured in β decay of ^{12}B and ^{12}N [21] of 10.3 ± 0.3 MeV and 3.0 ± 0.7 MeV and those obtained from a ^6Li study [11].

The angular distribution of the ratio of the elastic scattering cross section to Rutherford scattering is shown in Fig. 6. Angular distributions of inelastically scattered α particles exciting the 4.44 MeV 2^+ and 9.64 MeV 3^- states are shown in Fig. 7. The cross sections obtained for the 7.65 and 10.3 MeV 0^+ states are shown in Fig. 8 along with the angular distribution obtained for the 10.84 MeV 1^- state. Reliable cross sections could not be obtained for the 10.84 MeV state above $\sim 7.5°$, due to difficulties in separating this low intensity peak from other peaks. Generally cross sections obtained on different runs were in excellent agreement. Alpha particles scattering off hydrogen (presumably from H_2O) in the target in runs 1 to 4 obscured the peaks from several states at various angles. The graphite target used in run 5 showed no hydrogen contamination and data obtained in run 5 filled these gaps.

IV. DWBA AND OPTICAL MODEL ANALYSIS

Inelastic α scattering to collective states has been analyzed using either the deformed potential model or the folding model. Beene *et al.* [22] have shown that consistent agreement between electromagnetic transition strengths and those measured with light and heavy ion inelastic scattering for low lying 2^+ and 3^- states can only be obtained using
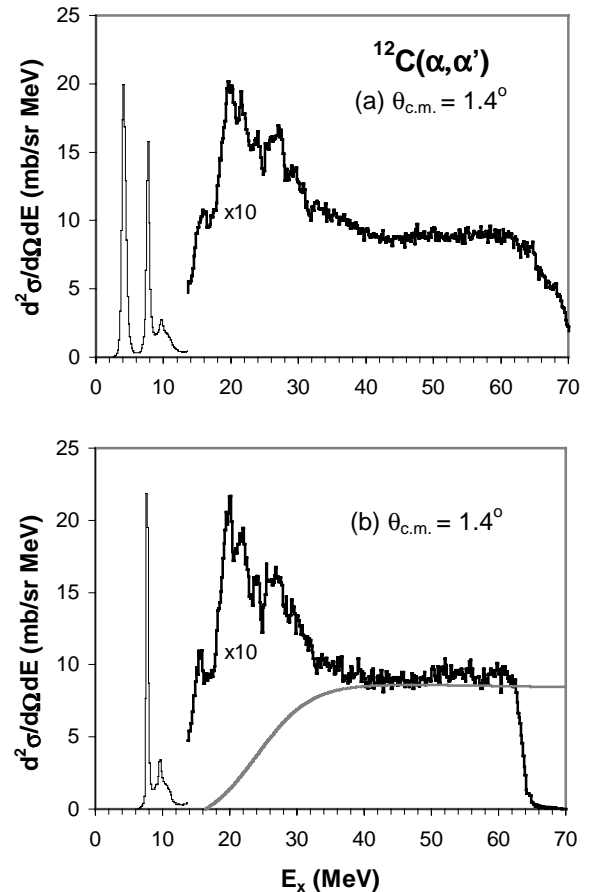

FIG. 4. α spectra obtained for $^{12}C(\alpha, \alpha')$ at $E_\alpha = 240$ MeV at $\theta_{c.m.} = 1.4°$ in (a) run 2 and (b) run 5. The cross section above $E_x = 13.7$ MeV has been multiplied by a factor of 10. The smooth line shown in (b) indicates the division between the continuum and the GR peak used in the analysis.

the folding model. In this study we extract $E0$, $E1$, $E2$, and $E3$ strength using a density dependent single folding calculation with a Woods-Saxon imaginary term (DDWS) of the type described by Satchler and Khoa [23] who used an α-nucleon interaction with a Gaussian form and a range $t_{\alpha-n} = 1.88$ fm.

Elastic and inelastic scattering folding model calculations were carried out with the code PTOLEMY [24]. The shapes of the real parts of the potentials and form factors for PTOLEMY were obtained using the codes SDOLFIN and DOLFIN [25]. The shapes (Woods-Saxon) of the imaginary part of the form factors were calculated externally and read into PTOLEMY for all L values. Input parameters for PTOLEMY were modified [26] to obtain a relativistic kinematically correct calculation. Collective model transition densities and sum rules for various multipolarities are described thoroughly in Refs. [13], [23], and [27–29]. It has been pointed out [13] that the transition density given by Harakeh and Dieperink [29] for the ISGDR in their Eq. (4) is for only one of the magnetic substates and must be multiplied by $(2l+1)^{1/2}$ to represent excitation of the ISGDR by α particles.

In attempting to fit the elastic scattering data, two different forms for $\rho(r)$ were tried in the present work. First, a
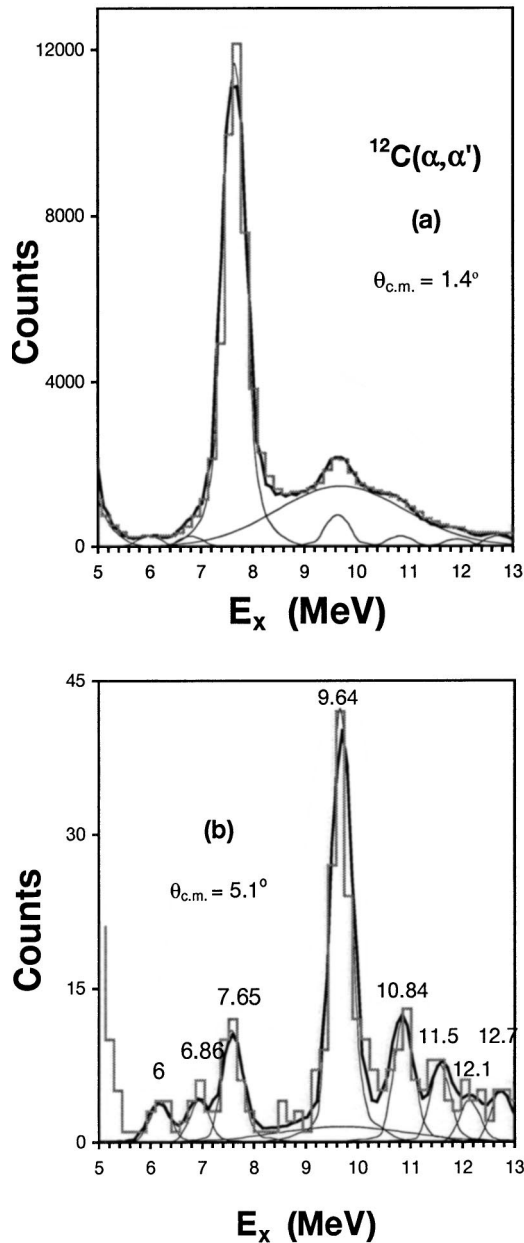
FIG. 5. α spectra obtained for ^{12}C(α,α') at $E_\alpha = 240$ MeV at two center of mass angles are shown for a limited E_x range by the histograms. The average center of mass angles are indicated in the panels. Least squares fits to the spectra used to obtained peak areas are shown by the bold lines. The thin lines show the individual peaks used in the fits.

Fermi form was used which has half density radius $c = 2.0005$ fm and diffuseness parameter $a = 0.5234$ fm and was shown [30] in 1995 to describe the ^{12}C charge distribution obtained in electron scattering experiments. With this form, the surface thickness ($t = 4a\ln 3$) of the ^{12}C nucleus is 2.3 fm, more than its half density radius. Second, a Parabolic Gaussian form given by $\rho(r) = \rho_0[1 + (4r^2/3a_N^2)]\exp(-r^2/a_N^2)$ where $a_N = 1.64$ fm, derived from oscillator functions, was used. This form was shown to fit elastic electron scattering up to $q \sim 2.5$ fm^{-1} in 1956 [31]. Satisfactory fits to the elastic scattering could not be obtained with either of
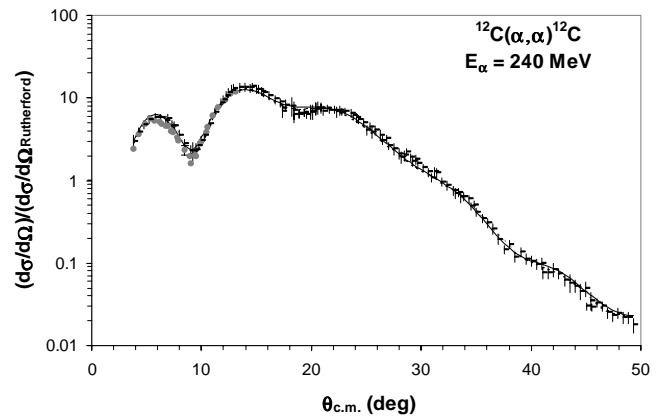

FIG. 6. The angular distribution of the ratio of the differential cross section for elastic scattering to Rutherford scattering for 240 MeV α particles + ^{12}C is plotted versus average center-of-mass angle. The horizontal semi-bars are data from run 4 and the gray circles are from run 5. For the latter, only a typical error bar is shown. The continuous and dashed lines show folding optical model calculations with the Fermi and Parabolic Gaussian forms of the ground state densities, respectively.

these density distributions with an α-nucleon range parameter $t_{\alpha-n} = 1.88$ fm, the value successfully used by Satchler and Khoa [23] and in several 240 MeV α studies of heavier nuclei [13–15]. Good fits could be obtained with both distributions with $t_{\alpha-n} = 1.75$ fm, however. The optical model parameters obtained with the two density distributions and $t_{\alpha-n} = 1.75$ fm are given in Table II. The calculated cross sections, which are almost identical, are shown in Fig. 6. A good
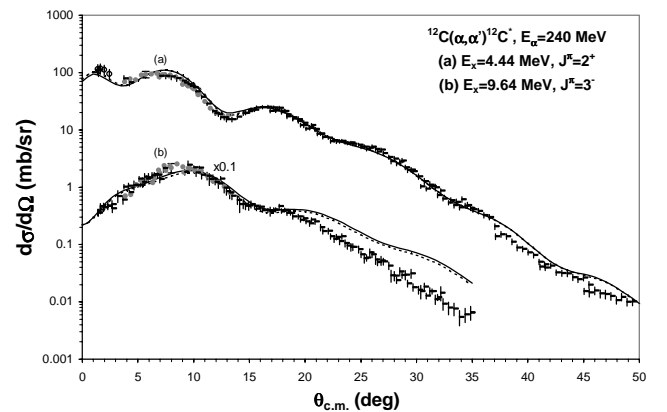

FIG. 7. The angular distribution of the differential cross section for inelastic α scattering exciting the (a) 4.44 MeV 2^+ and (b) 9.64 MeV 3^- states are plotted versus average center of mass angle. Data from runs 1, 4, and 5 are shown by the open circles, horizontal semibars and gray circles, respectively. In (b) data from run 2 and 3 are also shown by the horizontal semibars. Only a typical error bar is shown for the data from run 5. The continuous and dashed lines show DWBA calculations using the Fermi and Parabolic Gaussian forms for the ground state density, respectively. The data and the calculations for the 9.64 MeV state have been multiplied by 0.1. Values of $B(E2) = 0.00384$ e^2 b^2 and $B(E3) = 0.00024$ e^2 b^3 were used in the calculations for the 4.44 and 9.64 MeV states, respectively.
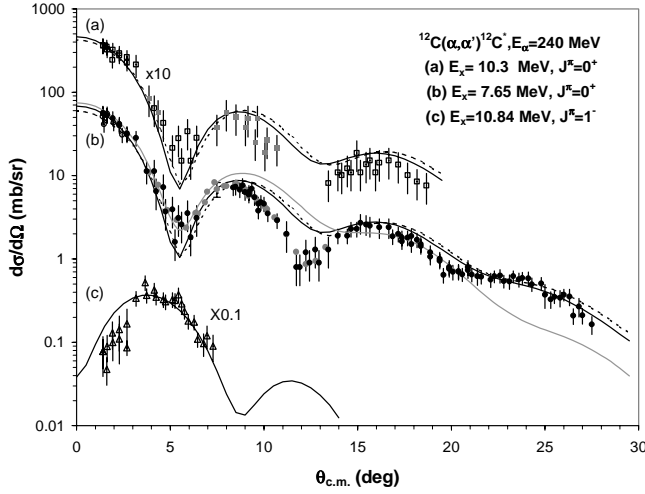
FIG. 8. The angular distributions of the differential cross section for inelastic α scattering to the (a) 10.3 MeV 0^+ state (squares), the (b) 7.65 MeV 0^+ state (circles), and the (c) 10.84 MeV 1^- state (triangles) are plotted versus average center of mass angle. The open circles in (b) are from run 1. The data from run 5 are colored gray. In (b) only a typical error bar is shown for the latter. The gray solid line in (b) shows a DWBA calculation using both real and imaginary components of the transition density, while the other calculations in (a) and (b) were carried out with the imaginary part of the transition density set to zero (see text). The continuous lines show DWBA calculations using the Fermi form for the ^{12}C ground state density while the dashed lines result from using the parabolic Gaussian form for the ground state density. Calculations for the 10.3 MeV state used $\beta_0 R = 0.315$ fm while those for the 7.65 MeV state used $\beta_0 R = 0.374$ fm and those for the 10.84 MeV state used $\beta_1 R = 0.051$ fm. The data and the calculations for the 10.3 MeV state have been multiplied by 10 and those for the 10.84 MeV state have been divided by 10.

fit with $t_{\alpha-n} = 1.88$ fm could be obtained with Fermi parameters $c = 2.1545$ fm and $a = 0.425$ fm, however the rms radius obtained with these parameters is significantly lower than the experimental value.

DWBA calculations for the 4.44 MeV 2^+ state, with Fermi and Parabolic Gaussian ground state densities are nearly identical and fit the data well out to about 37° as can be seen in Fig. 7. The $B(E2)$ value obtained by a least squares fit for both the ground state density forms was 0.00384 e^2 b^2. DDWS-DWBA calculations for the 9.64 MeV 3^- state are shown in Fig. 7 for both the Fermi and parabolic Gaussian ground state densities. Again, use of the two ground state densities result in very similar cross sections over the entire angle range and a $B(E3) = 0.00024$ e^2 b^3 re-
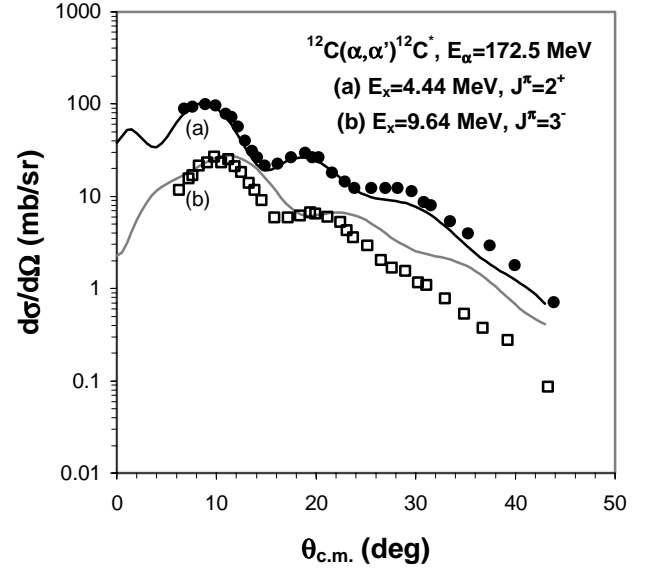

FIG. 9. Data from ^{12}C(α, α') at $E_\alpha = 172.5$ MeV from Ref. [32] is shown. The angular distributions of the differential cross section for inelastic alpha scattering to the 4.44 MeV 2^+ (closed circles) and for the 9.64 MeV 3^- states are plotted versus average center of mass angle. (a) The black line shows an $L=2$ DWBA calculation for $B(E2) = 0.0044$ e^2 b^2 using the Fermi form of ^{12}C ground state density. (b) The gray line shows an $L=3$ DWBA calculation for $B(E3) = 0.00038$ e^2 b^3 using the Fermi form of ^{12}C ground state density.

sults in a fair fit to the data inside 17°. Above 17°, the calculated cross section grows systematically larger than the data, and by 34° is three times the experimental cross section.

Kiss *et al.* [32] reported elastic and inelastic scattering on ^{12}C with a 172.5 MeV α-particle beam in 1987, and performed a deformed potential analysis of their data. For a direct comparison with our results we carried out a DDWS analysis of their data, first obtaining optical parameters by fitting the elastic scattering, then carrying out calculations for the 4.44 and 9.64 MeV states using DDWS-DWBA with the Fermi ground state density, and the results are shown in Fig. 9. An angle shift of 0.3° was required to obtain a good fit to the elastic scattering and is included in Fig. 9. The best fit $B(E2)$ obtained for the 4.44 MeV state is listed in the middle column of Table III and is in agreement with our value. The DDWS-DWBA calculation does not fit the data well for the 9.64 MeV 3^- state, however, $B(E3) \sim 0.00038$ e^2 b^3, substantially larger than the value from our data, provides the best normalization to the first maximum. The $B(EL)$ values

TABLE II. Folding model and ground state density distribution parameters used.

V (MeV)	W (MeV)	R_i (fm)	a_i (fm)	R_c (fm)	c (fm)	a (fm)	a_N (fm)	Density form
58.431	24.208	3.597	0.548	2.976	2.0005	0.5234		Fermi
55.201	23.172	3.598	0.550	2.976			1.64	Parabolic-Gaussian

TABLE III. $B(EL)$ values obtained for the 4.44 MeV 2^+ and the 9.64 MeV 3^- states in ^{12}C.

| | $B(EL)$ (e^2 b^L) | | |
| | α scattering analysis | | Electron scattering analysis |
E_x(MeV); J^π	Present data	Data from Ref. [32].	
4.44; 2^+	0.00384(52)	0.00435(40)	0.00397(33)[a]
9.64; 3^-	0.00024(4)	0.00038	0.00061(9)[b]

[a]Reference [33].
[b]Reference [34].

obtained from both of the above analyses are compared in Table III to those obtained in analyses of electron scattering data [33,34]. The three results are in excellent agreement for the 4.44 MeV 2^+ state. However, for the 9.64 MeV 3^- state, the $B(E3)$ values obtained from the two α scattering experiments do not agree but both are substantially below the electron scattering result. As excellent agreement has been obtained between electromagnetic experiments and α experiments analyzed with the folding model for 3^- states in heavier nuclei [13,15] and the calculated angular distributions for the 9.64 MeV state also do not reproduce the experimental distributions for either α particle energy, it would appear this state is not described well by the collective model.

DDWS-DWBA calculations for the 7.65 MeV 0^+ state with a deformation length of 0.353 fm using a breathing mode transition density and the Fermi ground state density are shown superimposed on the data in Fig. 8. The calculation is in agreement with the data near the first maximum and first minimum but differs substantially in the 10° to 15° range as well as above 20°. Calculations with a deformation length of 0.374 fm with the imaginary part of the transition potential set to zero (shown also in Fig. 8) fit the data much better over the entire angle range, although there is still some disagreement in the 10° to 15° range. The angular distribution obtained for the 10.3 MeV 0^+ state with the imaginary part of the transition potential set to zero is also in reasonable agreement with the data and is shown in Fig. 8. Angular distributions obtained for both 0^+ states using the parabolic Gaussian ground state density are very similar to those obtained with the Fermi density and are also shown in Fig. 8. The $E0$ strengths obtained for these states using the Fermi ground state density and breathing mode transition densities with the imaginary part set to zero are given in Table IV and (for the 7.65 MeV state) compared to other studies. The 7.65 MeV state is known to have a $3-\alpha$ cluster structure, which could significantly affect the strength seen in inelastic α scattering, however the angular distribution would be expected to be primarily characteristic of the angular momentum transfer and thus provides a good test of the ability of the DWBA calculations to represent an $L=0$ angular distribution.

DDWS-DWBA calculations were carried out for the 10.84 MeV 1^- state using the isoscalar dipole transition density and the Fermi ground state density and are shown in Fig. 8. The calculations fit the data fairly well. The isoscalar $E1$

TABLE IV. Isoscalar $E0$ and $E1$ energy weighted sum-rule strengths for low-lying states in ^{12}C.

| | Isoscalar EWSR (%) | | | |
E_x(MeV); J^π	Present work	^{3}He scattering analysis[a]	^{6}Li scattering analysis[b]	Electron scattering analysis[c]
7.65; 0^+	7.6±0.9	8.6	9.5	15
10.3; 0^+	6.9±0.9		5±1	
10.84; 1^-	0.08±0.02			

[a]Reference [10].
[b]Reference [11].
[c]Reference [37].

strength obtained is given in Table IV.

The deformation parameters obtained using the Fermi ground state density are listed in Table V for the first five excited states along with values reported in the literature. In the other studies, deformation lengths were obtained using the deformed potential model which has been shown [22] to require L-dependent renormalization to agree with EM and folding model results. For the 4.44 MeV 2^+ and 9.64 MeV 3^- states, deformed potential deformation lengths are lower than the folding model results by factors of 0.81 and 0.61, respectively, consistent with the observation made in Ref. [22].

Since the folding model calculations using the Fermi and Parabolic Gaussian ground state densities gave similar distributions and strengths, only the results with the Fermi ground state density are quoted in Tables III–V. DDWS-DWBA calculations for the high lying states were carried out using only the Fermi ground state density. As substantially better fits to discrete 0^+ states were obtained with the imaginary part of the transition potential set to zero, calculations for high lying 0^+ states were made with the same assumption.

V. DISCUSSION

Giant resonance peaks can be seen extending up past $E_x = 35$ MeV in the spectra shown in Fig. 4. Because pickup-breakup contributions to α particle yields are expected above an equivalent excitation energy of 45 MeV, our analysis was limited to $E_x < 45$ MeV. Multipole decomposition below this energy was carried out under two different assumptions, First, a continuum arising from non-resonant reactions was assumed to have the shape of a straight line at high excitation joining onto a Fermi shape at low excitation to model particle threshold effects [14]. Parameters of the continuum were chosen such that the continuum cross sections were zero below $E_x = 16.5$ MeV and rose to half maximum around $E_x = 24$ MeV to follow closely the continuum shape found in an experimental study of continuum structure of ^{12}C [35]. Such a continuum is shown in Fig. 4. Yield above this line was analyzed as part of the GR peak. The multipole components of the peak and continuum were obtained separately by dividing the spectrum into multiple regions (bins) by excitation energy and then comparing the angular distributions ob-

TABLE V. Deformation length and deformation parameter values obtained for low-lying states in ^{12}C (errors do not include approximately 10% systematic uncertainty due to uncertainties in absolute cross section).

E_x(MeV); J^π	$\beta_l R$ (fm)	β_l	$\beta_l R$ (fm)	β_l	$\beta_l R$ (fm)	β_l	$\beta_l R$ (fm)	β_l	$\beta_l R$ (fm)	β_l	$\beta_l R$ (fm)	β_l
4.44; 2^+	1.506±0.098	0.753±0.049			1.08	0.41		0.3	1.31		1.27	0.46
7.65; 0^+	0.374±0.026	0.187±0.013	0.31									
9.64; 3^-	1.115±0.132	0.556±0.066	0.56		0.67	0.26		0.18			0.68	0.24
10.3; 0^+	0.315±0.021	0.157±0.011										
10.84; 1^-	0.051±0.010	0.026±0.005	0.05									
E_α(MeV)	240		240		172.5		166		147		139	
Reference	Present work		[12]		[32]		[39]		[40]		[41]	

tained for the peak and continuum for each of these bins to DWBA calculations. In a second analysis described in the appendix, the cross section from nonresonant reactions was assumed to be zero at all energies and a multipole component analysis of the entire yield divided into energy bins was carried out as in the first method.

Angular distributions were obtained over the range 7 MeV$\leq E_x \leq$45 MeV for energy bins of width 0.475 MeV and examples are shown in Fig. 10. The first four angular distributions shown are in the energy region where the continuum was taken to be zero. For $E_x \geq$16.5 MeV, continuum angular distributions are also shown in Fig. 10. The data obtained in GR runs 2–5 were combined to obtain the peak and continuum angular distributions. Due to angle and detector dependent threshold effects data were not available from GR runs at larger angles below E_x=12.5 MeV.

DDWS-DWBA calculations for the various multipoles, with strengths adjusted to obtain a sum angular distribution that fit the experimental angular distribution are shown in Fig. 10 as lines. The isovector dipole resonance, excited only by Coulomb excitation in ^{12}C, is much weaker than the other multipolarities and has no impact on this analysis. The uncertainty from the multipole fits was determined for each multipole by incrementing (or decrementing) that strength, then adjusting the strengths of the other multipoles to minimize total χ^2. This continued until the new χ^2 was one unit larger than the total χ^2 obtained for the best fit [13].

The (isoscalar) $E0$, $E1$, $E2$, $E3$, and $E4$ strength distributions and errors obtained from fits of peak angular distributions are shown in Figs. 11 and 12. The continuum angular distribution for the entire excitation range could be fitted primarily by a sum of $E1$ and $E2$ angular distributions with small amounts of other multipolarities. The $E1$ and $E2$ strengths obtained from fits to the continuum increase monotonically with excitation energy up to the E_x=45 MeV limit of the analysis, and the total $E1$(176%) and $E2$(108%) strengths exceeded the respective EWSR limits. Clearly reaction mechanisms other than multipole transitions are responsible for a significant part of the continuum and they result in a combination of $E1$ and $E2$ type angular distributions. The $E0$ strength obtained from fits to the continuum is 2.5±0.2% of $E0$ EWSR and lies entirely below E_x = 27 MeV [Fig. 13(a)]. This is consistent with a small error in constructing the continuum and therefore the $E0$ strengths

observed from the peak and continuum were added and the result is shown in Fig. 13(b). For the excitation range 13 MeV$\leq E_x \leq$45 MeV the total $E0$ strength observed is 27±5% of $E0$ EWSR [bold histogram in Fig. 13(b)] with a centroid of 21.9±0.3 MeV and an rms width of 4.8±0.5 MeV. Including the strengths observed for the states at 7.65 and 10.3 MeV (Table IV), the total $E0$ strength observed below E_x=45 MeV corresponds to 41±6% of the $E0$ EWSR. The $E0$ strength distribution obtained from the multipole analysis for E_x<13 MeV was fitted with two Gaussians having centroids at 7.68 and 9.6 MeV and widths of 0.5 and 2.5 MeV, respectively. The $E0$ strengths obtained in the fits were 6.7±1.0 and 5.9±1.0% of the EWSR for the first and second peaks, respectively. These results compared well with the analysis of the angular distributions for the 7.65 and 10.3 MeV states (Table IV), despite the difference in the method and angular range in the multipole analysis. A previously unknown 0^+ state (0_4^+) with a centroid of E_x=14.5 ±0.2 MeV, an rms width of 0.6±0.1 MeV and a strength of 0.4% of the $E0$ EWSR is apparent in the $E0$ distribution. Above this, $E0$ strength consists of broad overlapping peaks. This region was subdivided according to visible structure and the strengths are given in Table VI.

The isoscalar $E0$ strength reported in Ref. [12] obtained using the spectrum subtraction technique is also shown in Fig. 11(a) as a gray histogram. The shapes of the two distributions shown in Fig. 11(a) agree well for $E_x \leq$30 MeV, but the multipole analysis identified 24±4% of the $E0$ EWSR in the peak whereas the spectrum subtraction technique identified only 14.5±4.0% of the $E0$ EWSR.

A broad distribution of isoscalar $E1$ strength corresponding to 78±9% of the $E1$ EWSR was identified in the range 10 MeV$\leq E_x \leq$45 MeV with a centroid of 27.5±0.4 MeV and an rms width of 7.6±0.6 MeV [Fig. 11(b)]. The $E1$ strength distribution was subdivided into seven excitation energy regions according to the visible structure and the strengths for each region are given in Table VII. The errors quoted do not include uncertainties in the choice of the continuum. There are no previously reported measurements of high lying isoscalar $E1$ strength in ^{12}C.

Isoscalar $E2$ strength corresponding to 51±7% of $E2$ EWSR was located in the range 10 MeV$\leq E_x \leq$45 MeV with a centroid of 22.6±0.5 MeV and an rms width of 6.8±0.6
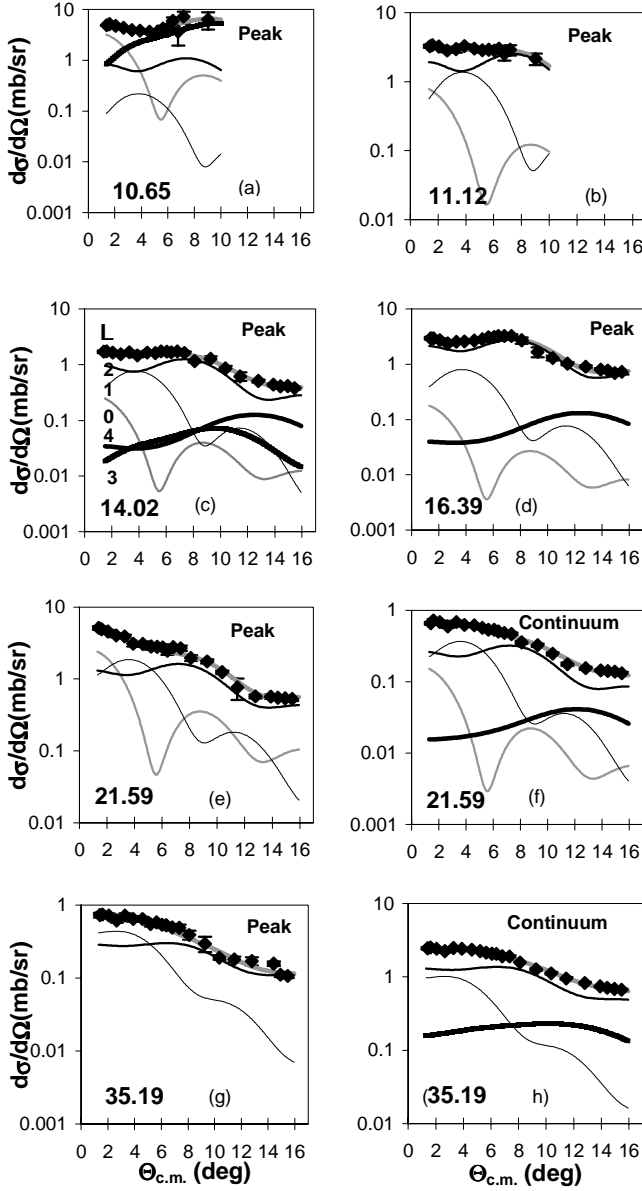
FIG. 10. Center-of-mass angular distributions of the differential cross section obtained in ^{12}C(α,α') at $E_\alpha = 240$ MeV are shown for six excitation ranges. Each excitation range is 475 keV wide and the average energies for each range are shown in the lower left corner of the panels in MeV. Panels (a)–(d) are in the excitation region where the continuum was zero. Panels (e)–(h) show two excitation regions where continuum angular distributions were also obtained. The error bars shown indicate the larger of the statistical errors or the standard deviations obtained in averaging the cross sections in the given energy and angle bins. The lines shown are the DWBA calculations. The thick gray lines passing through the data points shows the sum of all components. The component angular distributions are shown by lines of various weights and shades as $L=0$: gray line, $L=1$: thin black line, $L=2$: black line, $L=3$: thick heavy gray line, and $L=4$: thick black line.

MeV [Fig. 11(c)]. The distribution is composed of mostly of overlapping peaks. The first peak (the 2_2^+ state) has a mean energy $E_x = 11.46 \pm 0.2$ MeV, an rms width of 0.43 ± 0.10 MeV and a strength of $2.15 \pm 0.30\%$ of the $E2$ EWSR. The
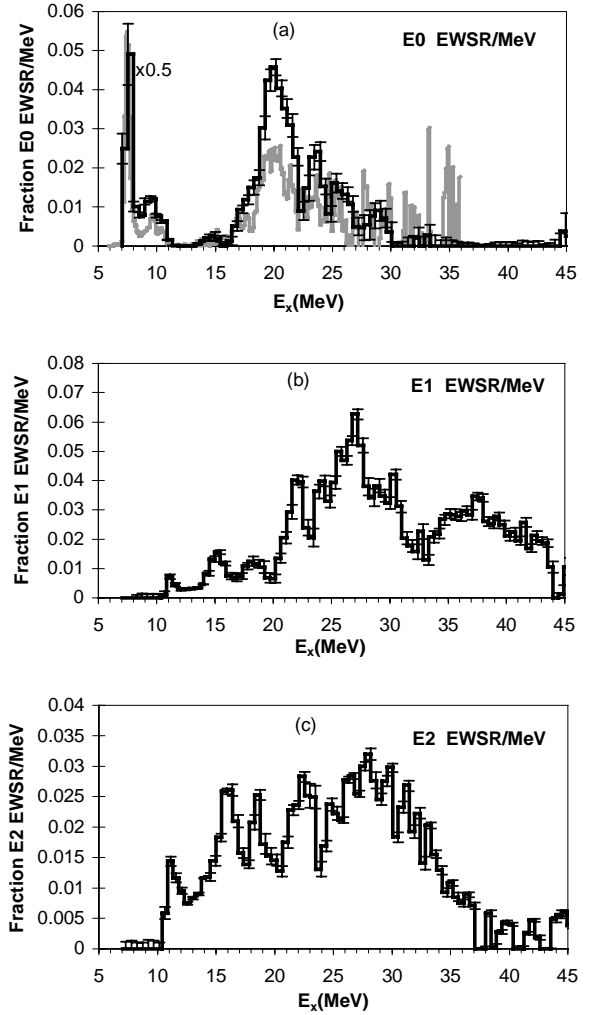

FIG. 11. The isoscalar $E0$, $E1$, and $E2$ strength distributions obtained from the analysis of the peak region in ^{12}C are shown by the histograms. The error bars shown represent the uncertainty due to the fitting of the angular distributions as described in the text. In (a), the $E0$ strength distribution reported for ^{12}C in Ref. [12] is shown by a gray histogram. The $E0$ strength distributions obtained for $E_x < 13$ MeV have been multiplied by 0.5.

$E2$ strength distribution was subdivided into five excitation energy regions according to the visible structure and strengths for each region are given in Table VIII. The location of the peaks agrees well with that reported in Ref. [32]. The strength reported in Ref. [32], obtained using a deformed potential model, is only about half of the strength found in the present work for the same excitation region. Similarly, in Ref. [9], less than 15% of the isoscalar $E2$ EWSR strength was found for 20 MeV$\leqslant E_x \leqslant$30 MeV using a deformed potential model whereas in this work, 24% of the $E2$ EWSR was found in the same excitation energy range.

Strength distributions obtained in the multipole analysis for $J^\pi = 3^-$ and 4^+ have more ambiguity compared to lower multipolarities. Angular distributions for multipolarities with $L \geqslant 4$ tend to be similar over the angle range measured. Moreover our multipole analysis did not include DWBA cal-
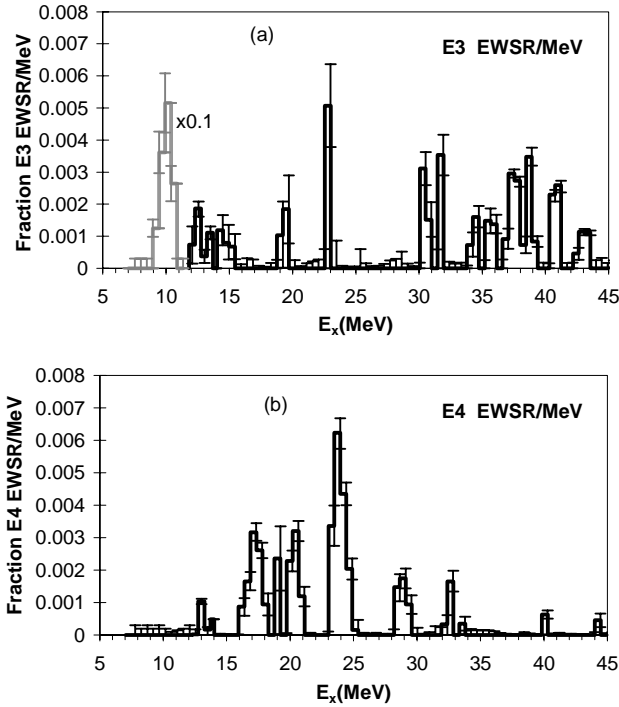
FIG. 12. The isoscalar $E3$ and $E4$ strength distributions obtained from the analysis of the peak region in ^{12}C are shown by the histograms. The error bars shown represent the uncertainty due to the fitting of the angular distributions as described in the text. The $E3$ strength distribution obtained for $E_x < 11$ MeV has been multiplied by 0.1 and is shown in gray.

culations for $L \geq 5$. Above $E_x = 12.5$ MeV, data were obtained up to 16°, which is sufficient to separate $E3$ strength from higher multipolarities. Below this energy, the limited angle range results in large errors for $L > 2$ distributions. However, the known 3^- state at 9.64 MeV and the 4^+ state at 14 MeV were identified in the multipole analysis. $E3$ and $L \geq 4$ strength can be distinguished from continuum processes in ^{12}C because the latter produce angular distributions dominantly of $E1$ and $E2$ type. Isoscalar $E3$ and $E4$ strength distributions obtained in the analysis are shown in Fig. 12, however as multipoles higher than 4 would be fit by $L = 4$ in our analysis, we label the result for $E4$ as $L \geq 4$, though the strength quoted was obtained assuming $E4$.

The strength obtained for the 9.64 MeV 3^- state from the multipole analysis was $6 \pm 1\%$ of $E3$ EWSR in agreement with $5.3 \pm 0.5\%$ obtained from the analysis of the peak angular distribution shown in Fig. 7. The 14.08 MeV 4^+ state is known to be a weak state [36] and the strength obtained from the multipole analysis was 0.023% of the $E4$ EWSR. Also, 0.049% of the $E4$ EWSR strength was identified in the region 13.0 MeV $\leq E_x \leq 13.7$ MeV, however a $T = 0$ state in this energy range ($E_x = 13.352$ MeV) is listed in Ref. [20] as a $2^-(T = 0)$ state. Others have suggested that this state is probably a 4^- state (Ref. [3], and references therein). Neither of these should be excited by α scattering. The $E3$ strength in the higher excitation region has not previously been reported, but the apparent narrow structure at high excitation is probably artifact. The very weak $E3$ and $E4$
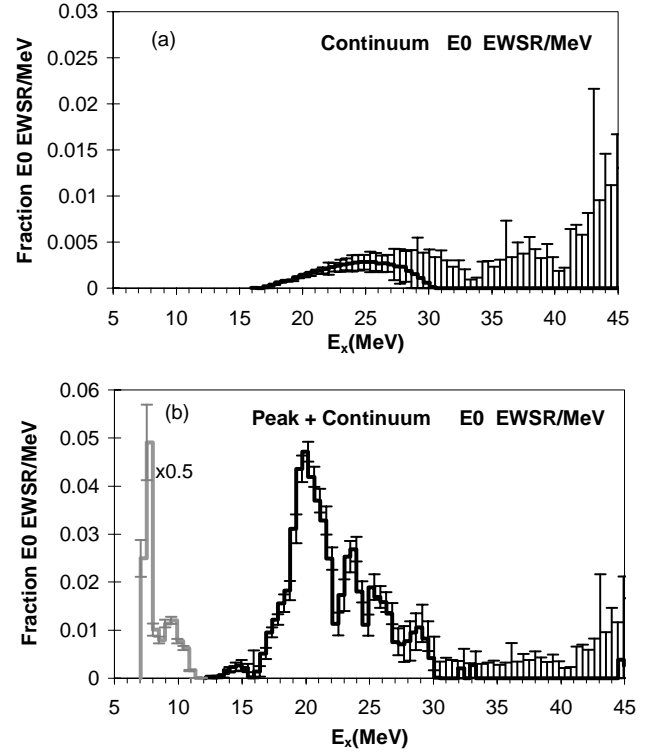

FIG. 13. (a) The isoscalar $E0$ strength distribution obtained from the analysis of the continuum is shown by the histogram. (b) The sum of $E0$ strength obtained from the analysis of the continuum and of the peak for ^{12}C is shown by the histogram. The strength distribution obtained for $E_x < 13$ MeV has been multiplied by 0.5 and is shown in gray color. The error bars shown represent the uncertainty due to the fitting of the angular distributions as described in the text.

strength would be extremely sensitive to fluctuations in the data. The total strength observed in the 12 MeV $\leq E_x \leq 45$ MeV region were 2.2 and 2.1 % of the EWSR for $L = 3$ and $L = 4$, respectively.

TABLE VI. Isoscalar $E0$ energy weighted sum rule strengths and energy moments obtained in the multipole analysis.

E_x range (MeV)	Mean E_x (MeV)	m_1/m_0 (MeV)	rms width (MeV)	$E0$ EWSR strength (%)
	7.68			6.66
	9.6		2.5 ± 0.4	5.89
13.0–15.46	14.48			0.45
15.46–22.55	19.92			15.68
22.55–24.9	23.56			4.38
24.9–27.72	25.97			4.01
27.72–30.07	28.80			1.89
30.7–45.0	38.82			0.46
13.0–45.0		21.9 ± 0.3	4.8 ± 0.5	27 ± 5
0.0–45.0[a]				41 ± 6

[a]Strengths for 7.65 MeV 0^+ and 10.3 MeV 0^+ from Table IV has been added in place of the values from the multipole analysis.

TABLE VII. Isoscalar $E1$ energy weighted sum rule strengths and energy moments obtained in the multipole analysis.

E_x range (MeV)	Mean E_x (MeV)	m_1/m_0 (MeV)	rms width (MeV)	$E1$ EWSR strength (%)
10.0–11.82	11.29			0.67
11.82–13.24	12.78			0.44
13.24–16.88	15.30			3.47
16.88–21.13	19.55			5.26
21.13–23.02	22.23			6.06
23.02–32.87	27.63			35.53
32.87–45.0	38.29			26.64
10.0–45.0		27.5±0.4	7.6±0.6	78±9
0.0–45.0				78±9

The "no continuum" analysis described in the appendix provides an indication of the sensitivity of the analysis to continuum choices. The $E0$ strength obtained is within errors the same as the sum of the peak and continuum analyses, indicating the $E0$ strength obtained is independent of continuum choice. The total $E1$ and $E2$ strengths obtained in the "no continuum" analysis far exceed the sum rule indicating that other processes are present whose angular distributions are being modeled by a sum of $E1$ and $E2$ distributions, and hence the $E1$ and $E2$ distributions obtained are quite sensitive to continuum choice. Below $E_x = 30$ MeV, the $E3$ and $E4$ distributions obtained were very similar in the two analyses, but substantial differences occurred above this energy, suggesting that the $E3$ and $E4$ distributions obtained above 30 MeV are sensitive to the continuum choice.

VI. CONCLUSIONS

In the present work using density dependent single folding, the $B(E2)$ obtained from inelastic α scattering exciting the 4.44 MeV 2^+ state in ^{12}C is in agreement

TABLE VIII. Isoscalar $E2$ energy weighted sum rule strengths and energy moments obtained in the multipole analysis.

E_x range (MeV)	Mean E_x (MeV)	m_1/m_0 (MeV)	rms width (MeV)	$E2$ EWSR strength (%)
10.0–12.29	11.46			2.15
12.29–17.35	15.42			8.19
17.35–20.19	18.90			5.03
20.19–23.96	22.31			8.02
23.96–45.0	30.44			28.0
10.0–45.0		22.6±0.5	6.8±0.6	51±7
0.0–45.0[a]				64±8

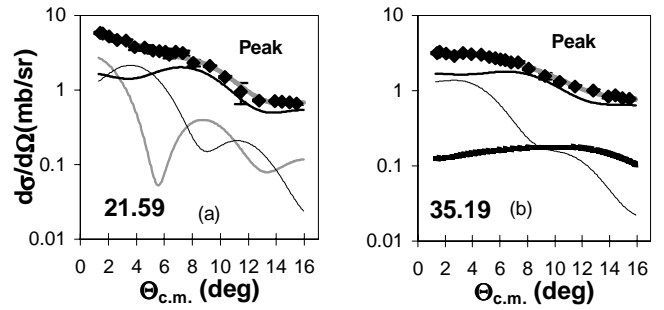[a]Strength for 4.44 MeV 2^+ from Table III has been added.

FIG. 14. Center-of-mass angular distributions of the differential cross section obtained assuming all strength is from multipole process is shown for two excitation ranges in ^{12}C along with DWBA fits. See Fig. 10 caption.

with the electromagnetic value, which is consistent with similar studies of heavier nuclei where $B(EL)$ values obtained by inelastic α scattering for low lying 2^+, 3^-, and 4^+ states were shown to agree with those obtained with electromagnetic probes. However the $B(E3)$ value obtained in this work for the 9.64 MeV 3^- state is much lower than that obtained by electron scattering (Table III) and the angular distribution is not well reproduced at angles above 20°. A folding analysis of 172.5 MeV inelastic α-scattering data reported in Ref. [32] also resulted in a $B(E3)$ much lower than the electron scattering result. Possibly the Bohr-Mottleson transition density [27] used is not appropriate for the 9.64 MeV state. The strength reported for 7.65 MeV 0^+ state from an electron scattering analysis [37] and the present analysis are also significantly different (Table IV), however this state is known to have a 3 α cluster structure and the breathing mode transition density would not be appropriate.

The 2_2^+ state was located at the lower end of a broad overlapping $E2$ strength distribution. The centroid and rms width of this state were determined to be 11.46 and 0.43 MeV, respectively. Since this state is not completely resolved from other $E2$ strength, further work may be necessary to decipher the exact energy and width of this state. Analysis performed for the region from 5 MeV $\leq E_x \leq 11$ MeV (Fig. 5) would have shown any collective 2^+ state with a strength above about 0.1% of $E2$ EWSR. It may be noted that the location of the 2_2^+ state is important for the models of rotational band built upon the 7.65 MeV 0^+ state. Particularly, its location gives direct information about the moment of inertia of this band. For example, the suggested linear three-α chain configuration for the 7.65 MeV 0^+ state suggests the expected 2_2^+ rotational state of the band to lie at about 8.6 MeV [5].

Significant $E0$, $E1$, and $E2$ strength was located in the range 13 MeV $\leq E_x \leq 45$ MeV, however, only small amounts of $E3$ and $L \geq 4$ strength were identified. Due to the limited angle range of our data, we could not unambiguously distinguish weak components for $L \geq 4$. Strength corresponding to only 27±5% of $E0$ EWSR was identified in the giant resonance region. This may be compared with 48, 72, 81, and 97 % of $E0$ EWSR found in the giant resonance region in ^{16}O [38], ^{24}Mg [15], ^{28}Si [13], and ^{40}Ca [14], respectively. It
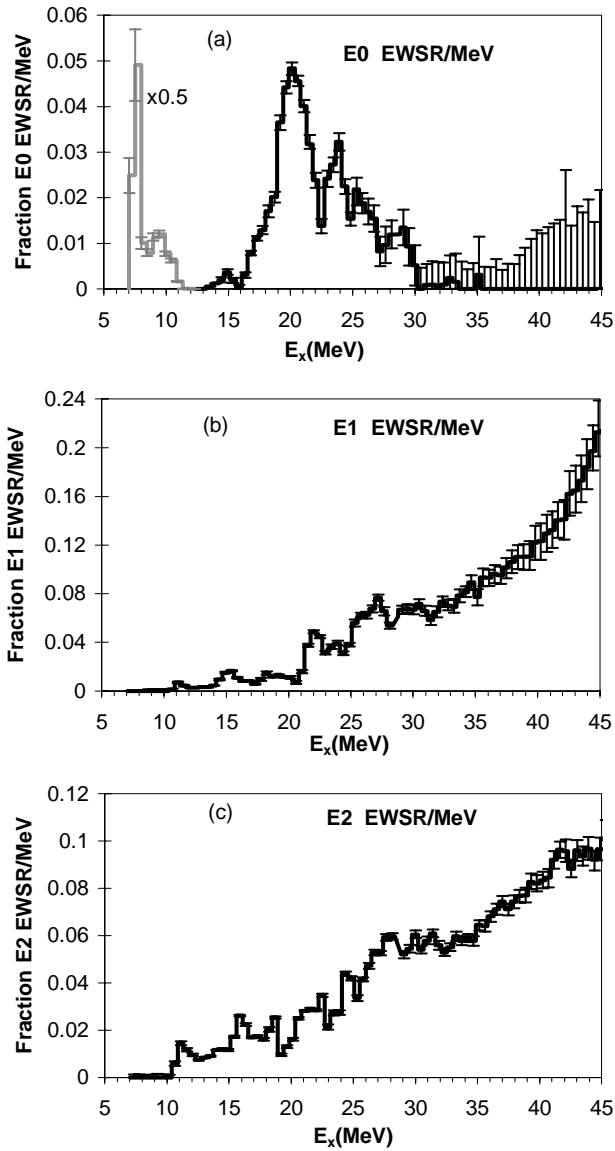
FIG. 15. The isoscalar $E0$, $E1$, and $E2$ strength distributions obtained assuming all the cross section is from multipole process for ^{12}C are shown by histograms. The error bars shown represent the uncertainty due to the fitting of the angular distributions as described in the text. The $E0$ strength distribution obtained for $E_x < 13$ MeV has been multiplied by 0.5 and is shown in gray color.

is possible that the breathing mode transition density is not an appropriate description of the high lying $E0$ strength in ^{12}C and hence that the magnitude of the $E0$ strength could be quite different from that obtained with this transition density.

About half of the expected $E2$ EWSR strength was identified in ^{12}C, most below $E_x = 35$ MeV, while a no-core nuclear shell model calculation with a realistic nucleon-nucleon interaction [4] predicted the GQR in ^{12}C in the $E_x = 37$ MeV to 47 MeV range. Less than 7% of the $E3$ EWSR strength was identified. The remainder of the $E3$ strength may lie at yet higher excitation but there exist no calculations to suggest the location of the strength.
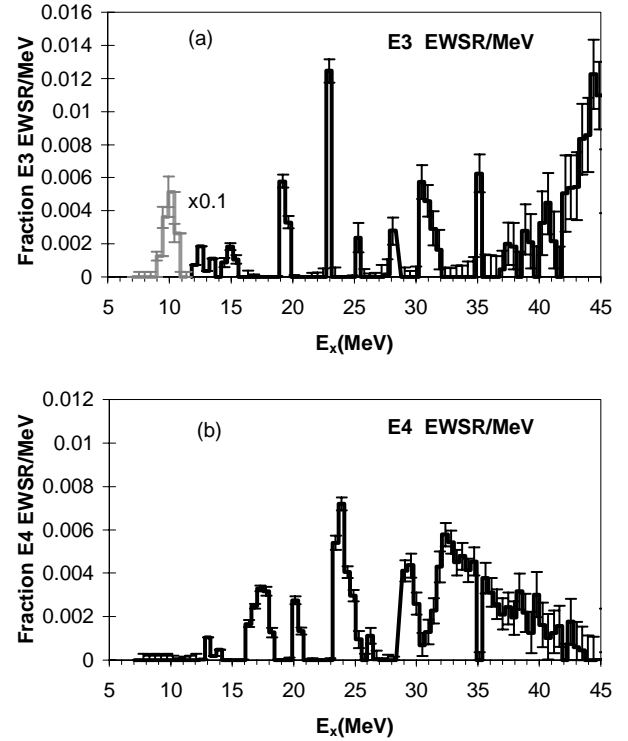

FIG. 16. The isoscalar $E3$, and $E4$ strength distributions obtained assuming all cross section is from multipole process for ^{12}C are shown by bold histograms. The error bars shown represent the uncertainty due to the fitting of the angular distributions as described in the text. The $E3$ strength distribution obtained for $E_x < 11$ MeV has been multiplied by 0.1 and is shown in gray color.

The isoscalar $E1$ strength identified in the peak corresponds to $78 \pm 9\%$ of the $E1$ EWSR in the range $10\,\text{MeV} \leqslant E_x \leqslant 45$ MeV. There are no previous reports on high lying $E1$ strength and no microscopic theoretical calculations have been reported for high lying isoscalar $E1$ strength in ^{12}C.

To summarize, we have determined $E0$, $E1$, $E2$, and $E3$ strength distributions in ^{12}C for excitation energy below 45 MeV, using small angle inelastic α-scattering. The collective folding model DWBA calculations used in the analysis took into account the role of the α-n effective interaction. The $B(E2)$ value determined for the first excited state is in agreement with electron scattering measurements. New data on the second and higher excited states were obtained. Substantial $E0$, $E1$, and $E2$ strength not previously seen was located in ^{12}C.

ACKNOWLEDGMENTS

APPENDIX

A multipole analysis was also carried out up to $E_x = 45$ MeV assuming that all of the cross section was due to

multipole processes with $L \leq 4$ (continuum equal to zero). Figure 14 shows the angular distributions and multipole fits obtained for two excitation energy bins corresponding to average $E_x = 21.59$ and 35.19 MeV. The multipole distributions obtained are shown in Figs. 15 and 16. The strengths observed are the same as in the other analysis for $E_x \leq 16.5$ MeV since the continuum was zero for this region in the other analysis. For $E_x \geq 16.5$ MeV, the $E0$ strength distribution obtained is very similar to that obtained in the other analysis and $30 \pm 5\%$ of the $E0$ EWSR was identified between 13 MeV $\leq E_x \leq 45$ MeV, in agreement with the 27% obtained analyzing the continuum and peak regions separately. The isoscalar $E1$ and $E2$ strengths obtained for 10 MeV $\leq E_x \leq 45$ MeV are 229 and 169 % of the respective EWSR. The $E1$ and $E2$ strengths rise rapidly at higher excitation, similar to that seen in the analysis of the continuum. The $E3$ and $L \geq 4$ distributions are similar to those obtained in the peak analysis for $E_x < 30$ MeV but for $E_x > 30$ MeV much more strength was indicated in this analysis. The total isoscalar $E3$ and $L \geq 4$

strength obtained in the 12 MeV $\leq E_x \leq 45$ MeV region was 6.3 and 6.0 % of the respective EWSRs', nearly triple that obtained in the analysis of the peak and continuum separately.

Differences in the multipole distributions obtained in the two analyses (with and without a continuum) provide an indication of the uncertainties due to the choices of the continuum. The $E0$ distributions obtained agree within the uncertainties of the fits, indicating that the $E0$ strength distribution obtained is essentially independent of continuum choice. Since the continuum is fit mostly by a sum of $E1$ and $E2$ angular distributions whose combined strengths considerably exceed the sum rule, these distributions are quite sensitive to the continuum choice. Below $E_x = 30$ MeV the $E3$ and $E4$ distributions obtained are very similar in the two analyses, indicating $E3$ and $L \geq 4$ strength obtained in this region is also not dependent on the continuum choice. Above this, the $E3$ and $E4$ strengths obtained were much larger (but still less than 7% of the EWSR) when the continuum was taken to be zero.

[1] J. P. Blaizot, Phys. Rep. **64**, 171 (1980).

[2] D. Vretenar, N. Paar, P. Ring, and T. Nikšić, Phys. Rev. C **65**, 021301(R) (2002).

[3] S. Karataglidis, P. J. Dortmans, K. Amos, and R. de Swiniarski, Phys. Rev. C **52**, 861 (1995).

[4] P. Navratil, J. P. Vary, and B. R. Barrett, Phys. Rev. Lett. **84**, 5728 (2000).

[5] R. R. Betts, Nuovo Cimento A **110**, 975 (1997).

[6] P. Descouvemont, Nucl. Phys. **A709**, 275 (2002).

[7] A. Tohsaki, H. Horiuchi, P. Schuck, and G. Röpke, Phys. Rev. Lett. **87**, 192501 (2001).

[8] I. Hamamoto, H. Sagawa, and X. Z. Zhang, Phys. Rev. C **57**, R1064 (1998).

[9] H. Riedesel, K. T. Knöpfle, H. Breuer, P. Doll, G. Mairle, and G. J. Wagner, Phys. Rev. Lett. **41**, 377 (1978).

[10] D. Lebrun, M. Buenerd, P. Martin, P. de Saintignon, and G. Perrin, Phys. Lett. **97B**, 358 (1980).

[11] W. Eyrich, A. Hofmann, A. Lehmann, B. Mühldorfer, H. Schlösser, H. Wirth, H. J. Gils, H. Rebel, and S. Zagromski, Phys. Rev. C **36**, 416 (1987).

[12] D. H. Youngblood, Y.-W. Lui, and H. L. Clark, Phys. Rev. C **57**, 2748 (1998).

[13] D. H. Youngblood, Y.-W. Lui, and H. L. Clark, Phys. Rev. C **65**, 034302 (2002).

[14] D. H. Youngblood, Y.-W. Lui, and H. L. Clark, Phys. Rev. C **63**, 067301 (2001).

[15] D. H. Youngblood, Y.-W. Lui, and H. L. Clark, Phys. Rev. C **60**, 014304 (1999).

[16] C. Angulo *et al.*, Nucl. Phys. **A656**, 3 (1999).

[17] D. H. Youngblood and J. D. Bronson, Nucl. Instrum. Methods Phys. Res. A **361**, 37 (1995).

[18] D. H. Youngblood, Y.-W. Lui, H. L. Clark, P. Oliver, and G. Simler, Nucl. Instrum. Methods Phys. Res. A **361**, 539 (1995).

[19] D. H. Youngblood, H. L. Clark, and Y.-W. Lui, Phys. Rev. C **57**, 1134 (1998).

[20] F. Ajzenberg-Selove and J. H. Kelly, Nucl. Phys. **A506**, 1 (1990). Update to NNDC.

[21] D. Schwalm and B. Povh, Nucl. Phys. **89**, 401 (1966).

[22] J. R. Beene, D. J. Horen, and G. R. Satchler, Phys. Lett. B **344**, 67 (1995).

[23] G. R. Satchler and D. T. Khoa, Phys. Rev. C **55**, 285 (1997).

[24] M. Rhoades-Brown, M. H. Macfarlane, and S. C. Pieper, Phys. Rev. C **21**, 2417 (1980); M. H. Macfarlane, and S. C. Pieper (unpublished).

[25] L. D. Rickertsen, The folding program DOLFIN, 1976 (unpublished).

[26] G. R. Satchler, Nucl. Phys. **A540**, 533 (1992).

[27] G. R. Satchler, Nucl. Phys. **A472**, 215 (1987).

[28] D. H. Youngblood, Y.-W. Lui, and H. L. Clark, Phys. Rev. C **55**, 2811 (1997).

[29] M. N. Harakeh and A. E. L. Dieperink, Phys. Rev. C **23**, 2329 (1981).

[30] G. Fricke, C. Bernhardt, K. Heilig, L. A. Schaller, L. Schellenberg, E. B. Shera, and C. W. DeJager, At. Data Nucl. Data Tables **60**, 177 (1995).

[31] J. H. Fregeau, Phys. Rev. **104**, 225 (1956).

[32] A. Kiss, C. Mayer-Böricke, M. Rogge, P. Turek, and S. Wiktor, J. Phys. G **13**, 1067 (1987).

[33] S. Raman, C. W. Nestor, Jr., and P. Tikkanen, At. Data Nucl. Data Tables **78**, 1 (2001).

[34] T. Kibédi and R. H. Spear, At. Data Nucl. Data Tables **80**, 35 (2002).

[35] J. A. Templon, B. A. Raue, K. Murphy, D. J. Millener, D. S. Carman, G. M. Huber, B. C. Markham, D. W. Miller, P. Schwandt, and L. C. Bland, Phys. Lett. B **413**, 253 (1997).

[36] K. W. Jones *et al.*, Phys. Rev. C **33**, 17 (1986).

[37] P. Strehl, Z. Phys. **234**, 416 (1970).

[38] Y.-W. Lui, H. L. Clark, and D. H. Youngblood, Phys. Rev. C **64**, 064308 (2001).

[39] B. Tatischeff and I. Brissaud, Nucl. Phys. **A155**, 89 (1970).

[40] K. T. Knöpfle, G. J. Wagner, A. Kiss, M. Rogge, C. Mayer-Böricke, and Th. Bauer, Phys. Lett. **64B**, 263 (1976).

[41] S. M. Smith, G. Tibell, A. A. Cowley, D. A. Goldberg, H. G. Pugh, W. Reichart, and N. S. Wall, Nucl. Phys. **A207**, 273 (1973).